

Blocking Lithium Dendrite Growth in Solid-State Batteries with an Ultrathin Amorphous Li-La-Zr-O Solid Electrolyte

Jordi Sastre (✉ Jordi.SastrePellicer@empa.ch)

Empa <https://orcid.org/0000-0003-0866-0911>

Moritz Futscher

Empa

Lea Pompizi

Empa

Abdessalem Aribia

Empa

Agnieszka Priebe

Empa

Jan Overbeck

Swiss Federal Laboratories for Materials Science and Technology <https://orcid.org/0000-0001-6401-2930>

Michael Stiefel

Swiss Federal Laboratories for Materials Science and Technology

Ayodhya Tiwari

Empa, Swiss Federal Laboratories for Material Science and Technology

Yaroslav Romanyuk

Swiss Federal Laboratories for Materials Science and Technology

Article

Keywords: solid electrolyte, lithium dendrites, amorphous LLZO, thin film coating

Posted Date: February 23rd, 2021

DOI: <https://doi.org/10.21203/rs.3.rs-219404/v1>

License:   This work is licensed under a Creative Commons Attribution 4.0 International License.

[Read Full License](#)

Version of Record: A version of this preprint was published at Communications Materials on July 14th, 2021. See the published version at <https://doi.org/10.1038/s43246-021-00177-4>.

Blocking Lithium Dendrite Growth in Solid-State Batteries with an Ultrathin Amorphous Li-La-Zr-O Solid Electrolyte

Jordi Sastre,^{*,†} Moritz H. Futscher,[†] Lea Pompizi,[†] Abdessalem Aribia,[†] Agnieszka Priebe,[‡] Jan Overbeck,[¶] Michael Stiefel,[¶] Ayodhya N. Tiwari,[†] and Yaroslav E. Romanyuk^{*,†}

[†]*Laboratory for Thin Films and Photovoltaics, Empa - Swiss Federal Laboratories for Materials Science and Technology, Überlandstrasse 129, CH-8600 Dübendorf, Switzerland*

[‡]*Laboratory for Mechanics of Materials and Nanostructures, Empa - Swiss Federal Laboratories for Materials Science and Technology, Feuerwerkerstrasse 39, CH-3602 Thun, Switzerland*

[¶]*Transport at Nanoscale Interfaces Laboratory, Empa - Swiss Federal Laboratories for Materials Science and Technology, Überlandstrasse 129, CH-8600 Dübendorf, Switzerland*

E-mail: jordi.sastrepellicer@empa.ch; yaroslav.romanyuk@empa.ch

Abstract

Lithium metal dendrites have become a roadblock in the realization of next-generation solid-state batteries with lithium metal as high-capacity anode. The presence of surface and bulk inhomogeneities with non-negligible electronic conductivity in crystalline electrolytes such as the lithium garnet $\text{Li}_7\text{La}_3\text{Zr}_2\text{O}_{12}$ (LLZO) facilitates the growth of lithium filaments, posing a critical safety risk. Here we explore the amorphous phase of

LLZO (aLLZO) as a lithium dendrite shield owing to its grain-boundary-free microstructure, stability against metallic lithium, and high electronic insulation. We demonstrate that by tuning the lithium stoichiometry in sputtered aLLZO films, the ionic conductivity can be increased up to 10^{-7} S cm $^{-1}$ while retaining an ultralow electronic conductivity of 10^{-14} S cm $^{-1}$. In Li/aLLZO/Li symmetric cells, plating-stripping results in no degradation of the films and current densities up to 3.2 mA cm $^{-2}$ can be applied with no signs of lithium penetration. The defect-free and conformal nature of the films enables microbatteries with an electrolyte thickness as low as 70 nm, which withstand charge-discharge at 0.2 mA cm $^{-2}$ for over 500 cycles. Finally, we demonstrate that the application of aLLZO as a coating on crystalline LLZO lowers the interface resistance and significantly impedes the formation of lithium dendrites, increasing the critical current density of a symmetric cell up to 1.3 mA cm $^{-2}$ at room temperature and without external pressure. The effectiveness of the amorphous Li-La-Zr-O as lithium dendrite blocking layer can accelerate the development of more powerful and safer solid-state batteries.

Keywords

solid electrolyte, lithium dendrites, amorphous LLZO, thin film coating

1 Introduction

Increasing power requirements in portable devices and the electrification of the automotive industry are pushing the demand for batteries with higher energy capacities and power rates. Solid-state batteries with Li metal as anode are foreseen as the next generation of energy storage devices, given the 10-fold higher capacity of Li metal with respect to traditional graphite anodes.^{1,2} Solid Li-ion conductive electrolytes, that potentially can enable such batteries, have been the subject of considerable interest in recent years. Among different families of solid electrolytes, the lithium garnet Li₇La₃Zr₂O₁₂ (LLZO) can be regarded as one

of the main contestants, owing to its high ionic conductivity up to 10^{-3} S cm⁻¹ and a wide electrochemical stability window, against metallic lithium and high potential cathodes.^{3,4} This ceramic electrolyte suffers however from a major drawback: Its polycrystalline nature makes it prone to the growth of lithium metal dendrites which can short circuit the battery.⁵⁻⁷ Although some debate is still ongoing in the research community, the main consensus points towards surface inhomogeneties, bulk defects and non-negligible electronic conductivities along the grain boundaries as the reason for lithium metal nucleation and dendrite growth through the solid electrolyte.⁸⁻¹⁰

Very recently, Kim et al. showed that a laser annealing treatment on a bulk LLZO pellet leads to the formation of an amorphized surface and this increases significantly the critical current density and lifetime of the electrolyte.¹¹ They claim that this in-situ formed amorphous surface blocks electron injection and hinders the formation of Li dendrites. However, the laser annealing procedure employed in that work does not allow to control and optimize the properties of the amorphous surface layer. In contrast, ex-situ coating processes such as physical vapor deposition (PVD) guarantee a well-controlled composition and better homogeneity. Kalita et al. first showed the feasibility of preparing amorphous Li-La-Zr-O thin films by RF magnetron sputtering and characterized the ionic conductivity of this material as a function of the sputtering power, reporting values in the order of 10^{-7} S cm⁻¹.¹² Garbayo et al. further investigated the amorphism in this type of electrolyte thin films prepared by pulsed-laser deposition (PLD) and revealed a relation between the ionic conductivity, the Li concentration and the formation of glassy states with regards to the processing temperature.¹³ These both studies highlighted the potential of the amorphous phase of LLZO, but did not go beyond characterizing stand-alone films nor demonstrated any application either in a thin-film battery configuration or as coating in a bulk solid-state battery. This leaves open the question whether the amorphous phase of LLZO could prevent the formation of Li dendrites, as it has been shown for other glassy electrolyte materials like Li₃PO₄ and its oxynitride analogous (LiPON).^{14,15}

In this work we present a thorough investigation of the chemical structure and electrochemical properties of amorphous Ga-doped Li-La-Zr-O (aLLZO) films prepared by magnetron sputtering. By tuning the excess lithium in the films, the ionic conductivity can be increased over three orders of magnitude, up to 10^{-7} S cm $^{-1}$, while retaining a negligible electronic conductivity of 10^{-14} S cm $^{-1}$. In this way it is possible to prepare ultrathin conformal and grain-boundary free films that can act as injection barrier for electrons while allowing Li ions to be transported across. The stability of the ultrathin films against metallic lithium is investigated by plating-stripping lithium in half and symmetric cells, showing no interfacial degradation and resistance to short circuits at currents up to 3.2 mA cm $^{-2}$. Finally, the applicability of this material is demonstrated in the form of surface coating to block formation of Li dendrites in bulk ceramic LLZO as well as ultrathin solid electrolyte for solid-state microbatteries, showing a functional battery with an unprecedented electrolyte thickness of 70 nm.

2 Results and discussion

2.1 Co-sputtering deposition of overlithiated Li-La-Zr-O thin films: phase and chemical structure

aLLZO thin films were deposited at room temperature by magnetron sputtering from a stoichiometric $\text{Li}_{6.25}\text{Ga}_{0.25}\text{La}_3\text{Zr}_2\text{O}_{12}$ target. To control the lithiation level of the amorphous film, a Li_2O target was simultaneously co-sputtered (as shown in Figure 1.a), allowing to tune the mass fraction of LLZO and Li_2O by controlling the sputtering power on each target. We previously used this method to compensate lithium losses in the preparation of crystallized LLZO thin films.^{16,17} Besides compensating lithium losses, it is an effective way to tune the Li-ion concentration in the electrolyte film and modify its electrochemical properties. To characterize the morphology, composition, ionic and electronic properties, films were prepared on Pt-coated Si and on insulating MgO single crystal substrates. As

seen in the cross-section secondary electron microscopy (SEM) image in Figure 1.b, the as-deposited films, with a thickness of about 70 nm, are homogeneous and conformally cover the substrate. The 3D tomogram in Figure 1.c shows the elemental structure of in the interior of the film reconstructed from a gas-assisted focused ion beam time-of-flight secondary ion mass spectroscopy (FIB-ToF-SIMS) measurement.¹⁸ The measurement reveals a uniform distribution of the matrix elements (La and Zr) of the aLLZO film coated on the Pt-coated Si substrate. Detailed plots of each element’s signal and a depth profile can be found in Figures S1 and S2.

In Figure 1.d the XRD diffractogram of the aLLZO film exhibits no sharp reflections but a broad hump, in contrast to the well-defined reflections in the LLZO film crystallized at 700 °C (cLLZO) that match well the reference pattern of cubic Ga-doped LLZO (ICSD 430603).¹⁹ This confirms the amorphous nature of the as-deposited films, with no long-range order in the crystal structure, and is consistent with the studies of Kalita et al.¹² and Garbayo et al.¹³ To further investigate the short-range order and chemical structure of the films, we performed Raman and Fourier-transform infrared (FT-IR) spectroscopy measurements on the films. The Raman spectra of the aLLZO film presented in Figure 1.e shows a predominant vibrational mode at 800 cm^{-1} that can be attributed to lithium peroxide Li_2O_2 .²⁰ This indicates that the formation of lithium peroxide is more thermodynamically favorable than other lithium oxide forms under the oxygen-rich, highly-energetic conditions of the sputtering deposition. Kim et al. also reported the presence of Li_2O_2 in the amorphized surface of laser-treated LLZO.¹¹ In contrast to the Raman spectrum of the crystallized LLZO sample also shown in Figure 1.e, the lack of any sharp peaks characteristic of the garnet crystalline structure further evidences the amorphous disordered structure present in the aLLZO films. Figure 1.f shows the FT-IR transmittance spectrum of the film. The lack of features in the region above 1000 cm^{-1} indicates that the film does not contain carbonate nor hydroxy compounds. In the region below 1000 cm^{-1} multiple absorptions can be observed, which can be attributed to the Zr,²¹ La,^{22,23} and Li²⁴ bonds with oxygen. Figure 1.g visualizes a

possible chemical structure consisting of a glass network of disordered Zr-O and La-O chains (network former) and weakly bonded Li cations (network modifier) that can freely migrate along the glassy network, in a similar fashion to other lithium-conductive amorphous oxide electrolytes previously reported.²⁵

2.2 Lithium-ion conductivity: the role of excess Li₂O

The ionic conductivity of the films was measured by through-plane impedance spectroscopy using silicon as substrate with Pt as back electrode and patterned Au top electrodes, as illustrated in the inset of Figure 2.a. A Nyquist plot of the impedance response of a selected sample is shown in Figure 2.a. The characteristic semicircle arising from the electrolyte response can be modeled with a Randles equivalent circuit,²⁶ yielding the electrolyte resistance from which the ionic conductivity can be derived. The tail at lower frequencies is due to the blocking nature of the electrodes and the resulting accumulation of charges at the interfaces. Figure 2.b shows the extracted ionic and electronic conductivities at 300 K for samples prepared with different mass fractions of LLZO and Li₂O, regulated by the sputtering rates of both target materials. Films prepared without any Li₂O show poor ionic conductivities below 1×10^{-11} S cm⁻¹. As the fraction of Li₂O is increased, the ionic conductivity increases by three orders of magnitude up to 1×10^{-7} S cm⁻¹ for a mass fraction of 0.66 LLZO:Li₂O. At lower LLZO:Li₂O mass fractions, the ionic conductivity decreases again although not as abruptly as in the low Li₂O fraction region. In contrast, the electronic conductivity remains fairly constant at 1×10^{-14} S cm⁻¹ for different mass fractions of LLZO and Li₂O, seven orders of magnitude below the best ionic conductivity measured and about six orders of magnitude below reported values for bulk and thin-film crystalline LLZO.^{8,17}

The ionic conductivity σ depends on both the density of mobile ions and their mobility and can be described with an Arrhenius relationship:

$$\sigma = qn\mu = qn\mu_0 \exp \frac{-E_a}{k_B T}$$

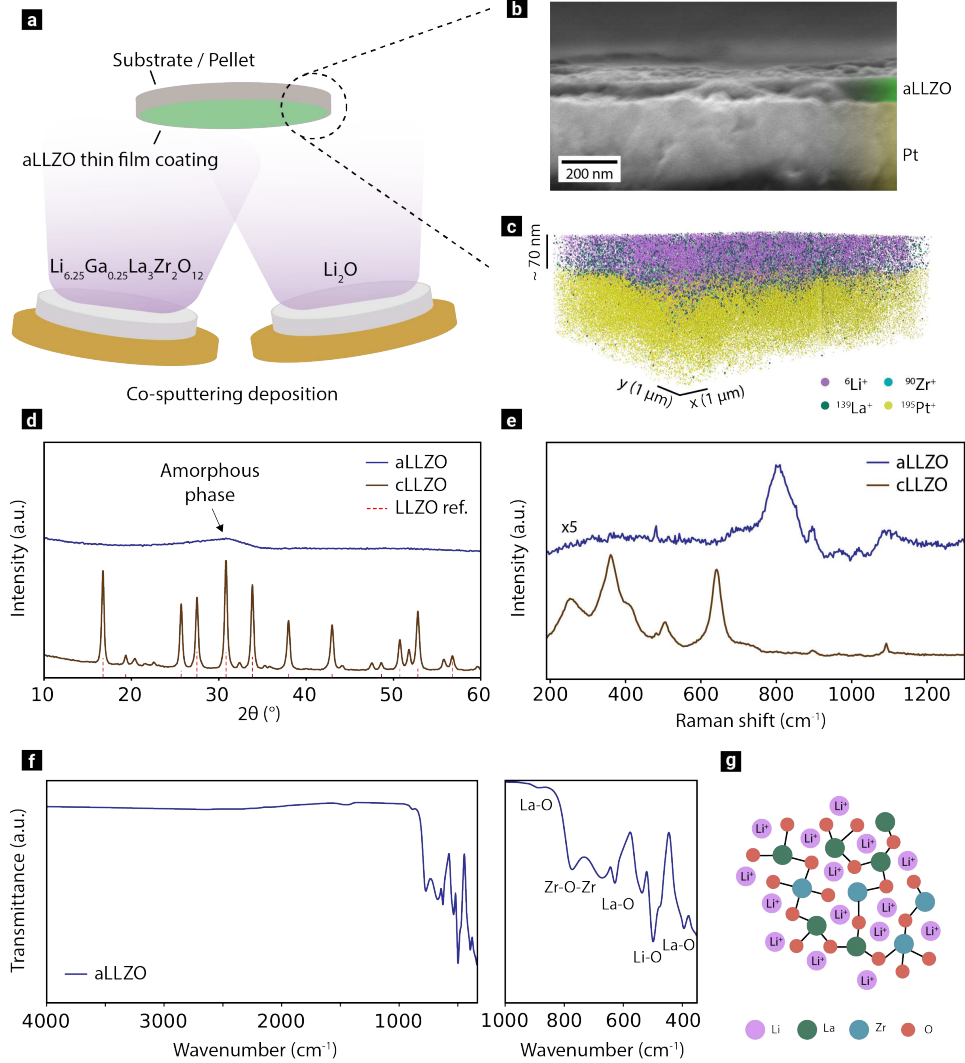


Figure 1: Morphological, phase and chemical characteristics of the amorphous Li-La-Zr-O ultrathin films. (a) Schematic of the co-sputtering deposition process employed to prepare overlithiated amorphous Ga-doped Li-La-Zr-O (aLLZO) coatings. (b) Cross-section SEM image of the aLLZO film on a Pt-coated Si substrate. (c) Elemental tomogram obtained by GIS-assisted FIB-ToF-SIMS of an aLLZO film deposited on Pt-coated Si. (d) XRD diffractograms of an aLLZO film and a crystallized LLZO (cLLZO) film on single-crystal MgO. A reference pattern for LLZO (ICSD 430603) is included. (e) Raman spectra of the aLLZO and crystallized LLZO films on MgO single crystal substrates. (f) FT-IR transmittance spectrum of the aLLZO film. (g) Representation of the chemical structure of the amorphous Li-La-Zr-O.

where E_a is the activation energy for ion migration, k_B the Boltzmann's constant, T the temperature, and μ_0 a pre-exponential factor.²⁷ To determine whether the change in ion conductivity is due to a change in the density or mobility of mobile ions, we performed

temperature dependent impedance spectroscopy and current transient measurements (see SI for details). We find that increasing the amount of Li_2O up to 33% of the total mass the increases density of mobile ions and decreases the activation energy, which increases mobility (Figure 2.c-e). Consequently, we assign the increased ionic conductivity to an increased amount of Li^+ ions, which reduces the electrostatic interaction between the disordered Zr-O and La-O chains and the mobile Li^+ ions, resulting in a decrease in activation energy. This is consistent with findings on other amorphous solid electrolytes such as lithium thiophosphate (LPS) and lithium phosphorus oxynitride (LiPON).²⁸ Above a critical mass fraction we assume that the added Li^+ ion forms aggregates which reduce the ion conductivity, as suggested by the obtained mobile Li^+ ion density, which does not increase further after the critical mass fraction of 0.66 LLZO: Li_2O is reached.

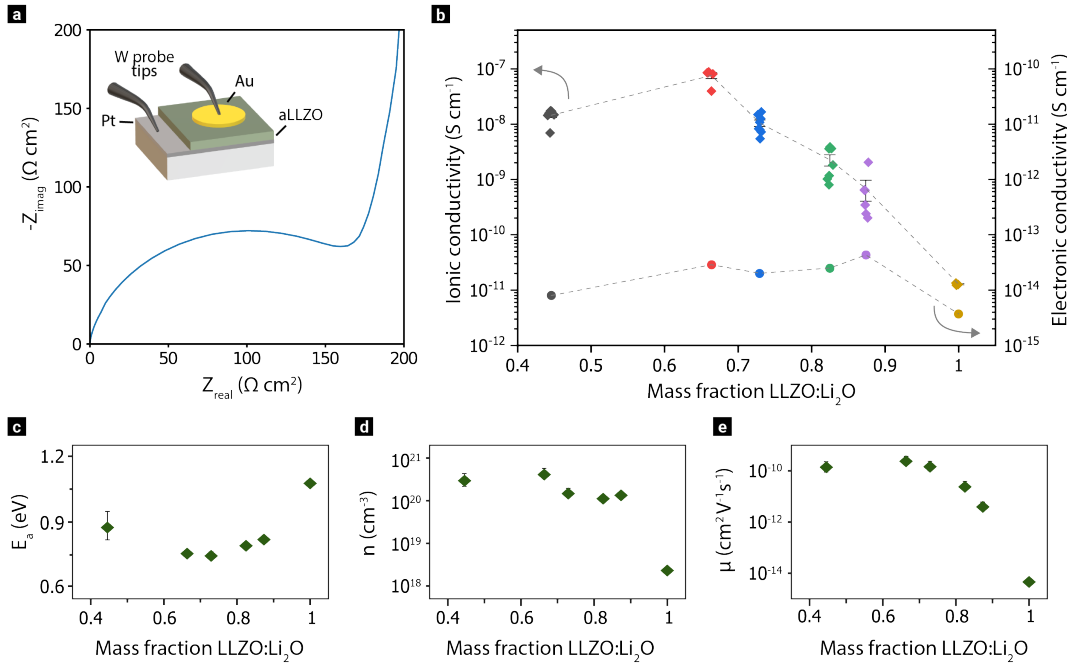


Figure 2: Ionic and electronic transport dynamics of the aLLZO ultrathin films. (a) Nyquist plot of the impedance spectra of an aLLZO film measured with blocking electrodes at room temperature. Inset shows a schematic of the device geometry. (b) Ionic and electronic conductivities of aLLZO films prepared with different mass fractions of LLZO and Li_2O . (c) Activation energy of the ionic conductivity, (d) mobile Li^+ concentration and (e) Li^+ mobility of aLLZO films with different amounts of Li_2O based on the mean of three measurements each.

2.3 Stability against lithium metal plating-stripping

The electrochemical stability of the aLLZO electrolyte was tested by fabricating a half cell with Pt as working electrode and metallic Li as counter and reference electrode. As presented in Figure 3.a, Li^+ was slowly transported towards the Pt electrode applying a low current of $1.25 \mu\text{A cm}^{-2}$ through the cell until approaching 0 V vs Li/Li⁺. The cell was galvanostatically cycled multiple times while measuring the impedance after each cycle in order to monitor any possible electrochemical degradation of the electrolyte as a result of the Li redox reactions. Figure 3.b shows the Nyquist plot of the impedance and the extracted electrolyte resistance measured during the plating-stripping process. The resistance of the aLLZO film slightly decreases in the first four steps and then it stabilizes at a constant value. The stabilization of the electrolyte resistance evidences electrochemical stability of the aLLZO electrolyte in combination with a Li anode.

The resistance of the aLLZO electrolyte against Li dendrite formation and short circuiting was tested in a symmetrical Li/Li cell, prepared by evaporating metallic Li on sapphire, coating the Li electrode with a thin aLLZO film and depositing a symmetric Li contact on top. The symmetric cells were cycled at increasing current densities, from 0.2 mA cm^{-2} up to 3.2 mA cm^{-2} , for 5 plating-stripping cycles each. For each current density, the transferred capacity was limited to 0.1 mA h cm^{-2} , equivalent to a Li thickness of 250 nm. Figure 3.c shows the voltage response of the symmetric cells upon Li stripping-plating at different current densities. The cell polarization remains stable and scales with the current density, without sign of large voltage fluctuations nor drops to 0 V which would indicate short-circuit formation. The area specific resistance of the symmetric cell is shown in Figure S7.

2.4 Dendrite-blocking coating on bulk crystalline LLZO

The stability against Li metal, dendrite penetration robustness, negligible electronic conductivity of $10^{-14} \text{ S cm}^{-1}$ and good ionic conduction of the aLLZO ultrathin films here investigated can also be applied as an interface coating for bulk ceramic solid electrolytes,

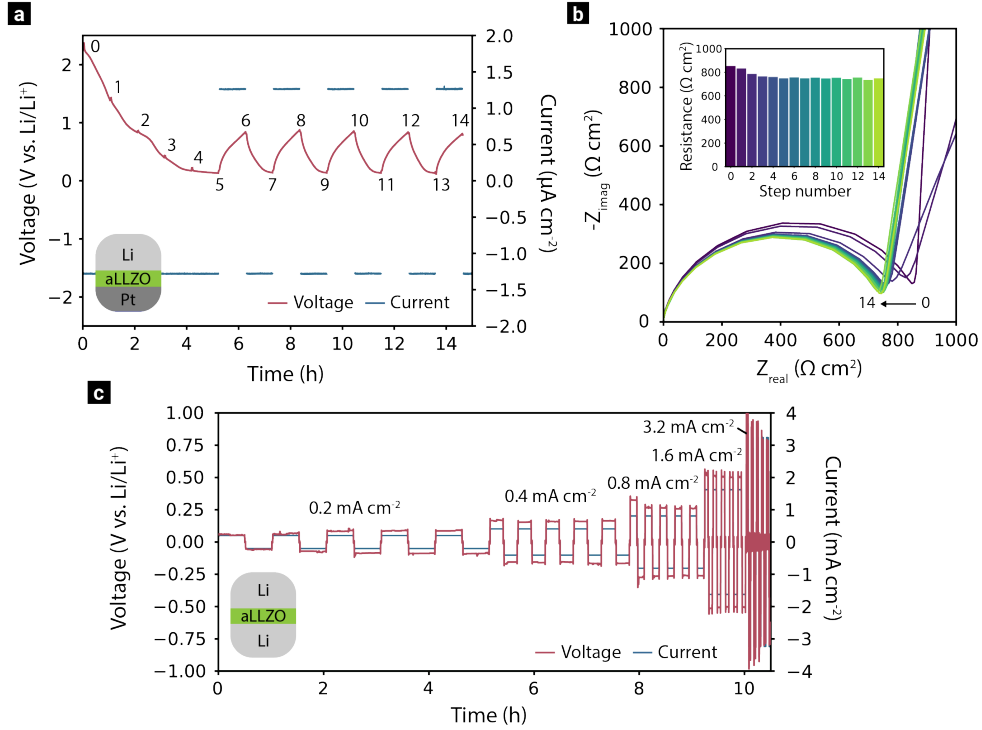


Figure 3: Li stability and short circuit resistance of the aLLZO films. (a) Galvanostatic response of an aLLZO electrolyte film upon electrochemical transport of Li⁺ from a Li counter electrode to a Pt working electrode and reversely. Numbers along the plot line indicate the points at which impedance spectroscopy measurements were carried out. (b) Nyquist plot of the impedance response of the aLLZO film in contact with Li metal after multiple steps of plating and stripping. Inset shows the evolution of the electrolyte resistance extracted from the impedance spectra. (c) Galvanostatic response of an aLLZO electrolyte film in a symmetric Li/Li cell configuration. Forward and reverse current densities ranging from 0.2 mA cm⁻² up to 3.2 mA cm⁻² were applied in steps of 0.1 mA h cm⁻².

which are employed to fabricate bulk solid-state batteries. The aLLZO interlayer blocks the injection of electrons to the grain boundaries, which prevents the reduction of lithium ions and the formation of lithium metal filaments,⁹ while allowing a fast ionic transport across the interface. In addition, the amorphous nature of the coating promotes a more homogeneous lithium nucleation at the anode interface, reducing the formation of voids and therefore leading to lower interface resistance and a more uniform distribution of the current.

To test the potential application of the ultrathin aLLZO as interface coating to hinder lithium dendrite formation in bulk ceramic electrolyte, symmetrical cells with crystalline Ga-doped LLZO pellets coated on both sides with a 10 nm aLLZO film were built as shown in

Figure 4.a. Figure 4.b shows the Nyquist plot of the impedance spectroscopy measurements at room temperature of both the aLLZO-coated and reference (uncoated) symmetric cells. The intercept with the real axis at high frequencies is attributed to the ionic conduction through the bulk. The value for the bulk resistance ($\sim 25 \Omega \text{ cm}^2$) is consistent with the bulk ionic conductivity of the LLZO pellet (about $1 \times 10^{-3} \text{ S cm}^{-1}$). The semicircles that appears in the Nyquist plot can be attributed to the interface resistance. In the case of the aLLZO-coated cell, one can estimate an interfacial resistance of $3.5 \Omega \text{ cm}^{-2}$, about half the value of that of the uncoated reference.

Li plating-stripping experiments were carried out by galvanostatically cycling the symmetric cells with current densities ranging from $5 \mu\text{A cm}^{-2}$ up to 5.1 mA cm^{-2} in steps of 30 min. The measurements were carried out at room temperature and without external pressure, a part from that of the alligator clamp used to contact the cell. Figure 4.c shows the voltage response and applied current density (dashed line) over time. As expected from the lower interfacial resistance, the aLLZO-coated sample shows significant less overpotentials than the uncoated one. For example, at $40 \mu\text{A cm}^{-2}$, the overpotential of the aLLZO-coated cell (2.5 mV) is half that of the uncoated reference cell. From 0.16 mA cm^{-2} , the overpotential of the uncoated cell starts to grow uncontrollably as a result of void formation at the Li/LLZO interface and lower contact area.⁵ Eventually, at a current density of 0.64 mA cm^{-2} , the uncoated cell shunts due to dendrite growth across the ceramic electrolyte. In the the aLLZO-coated cell, the overpotential profile remains stable up to a current density of 0.64 mA cm^{-2} and the cell does not start to form microshorts until the applied current density reaches 2.6 mA cm^{-2} . This experiment proves that the aLLZO coating improves the interface contact between lithium metal and crystalline LLZO and increases the critical current density (ie. the current density at which a short circuit is formed) by a factor of 4.

To visualize the formation of Li dendrites, an in-plane plating-stripping experiment with a crystalline LLZO pellet was carried out as illustrated in Figure 5.a. Half of the LLZO pellet

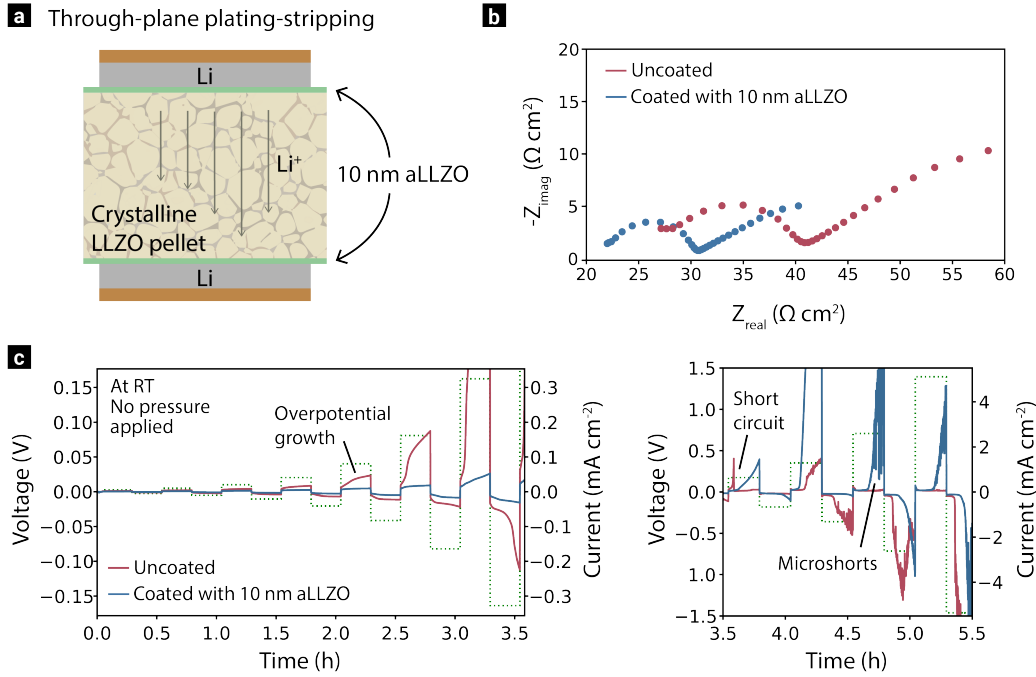


Figure 4: Ultrathin aLLZO coating inhibits the growth of Li dendrites in bulk crystalline LLZO electrolyte. (a) Schematic of the through-plane Li/aLLZO/LLZO/aLLZO/Li configuration employed to determine the critical current density. (b) Nyquist plot of the impedance response of the uncoated and aLLZO-coated LLZO pellets. (c) Applied current density (dashed line) and voltage response (solid lines) during symmetric galvanostatic cycling of the uncoated and aLLZO-coated LLZO pellets at RT without external pressure applied. Forward and reverse current densities ranging from $5 \mu\text{A cm}^{-2}$ up to 5.1mA cm^{-2} were applied in steps of 30 min.

surface was coated with a 10 nm aLLZO film (left side) and the other half was left uncoated as the reference (right side). Li metal/Cu contacts were deposited by thermal evaporation with different lateral separations, as seen in the optical image in Figure 5.a. As demonstrated by Kazyak et al.,²⁹ such an in-plane geometry is useful to visualize by in-operando microscopy the formation and propagation of Li dendrites in solid electrolytes. In our case it becomes useful to assess the effect of the aLLZO coating on the formation of Li dendrites.

Lithium plating-stripping was performed by applying currents in forward and reverse direction between both Li metal contacts. The current and voltage curves as a function of time is presented in Figure 4.c. The current density was increased step-wise from $50 \mu\text{A cm}^{-2}$ to 3.2mA cm^{-2} for a total charge transfer of $25 \mu\text{A h cm}^{-2}$, with 15 min rest steps in between.

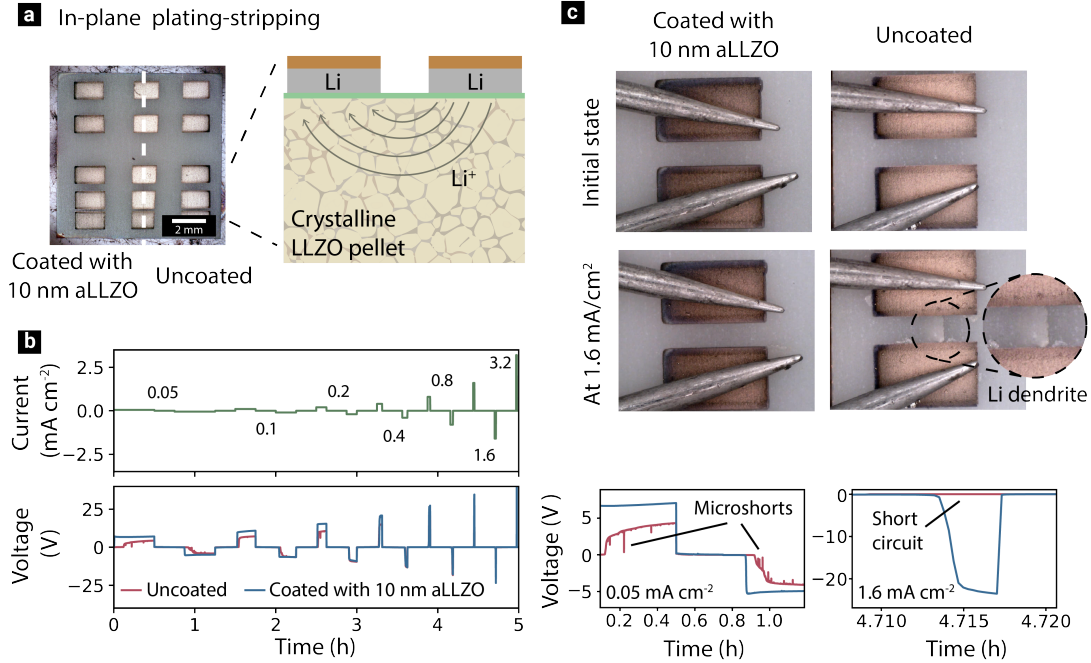


Figure 5: Visualizing dendrite growth in bulk crystalline LLZO electrolyte. (a) Optical picture and schematic of the in-plane geometry employed to visualize the formation of dendrites upon Li plating-stripping. Half of a 10×10 mm LLZO pellet was coated with 10 nm aLLZO and Li metal contacts with Cu as current collector were deposited on both sides of the pellet. (b) Nyquist plot of the impedance response between two of contacts spaced 0.5 mm on the aLLZO-coated side. (c) Current and voltage response during symmetric galvanostatic cycling between two Li metal contacts. Forward and reverse current densities ranging from 0.05 mA cm^{-2} up to 3.2 mA cm^{-2} were applied in steps of $25 \mu\text{A h cm}^{-2}$. Subplots show a zoom-in of the polarization in the uncoated and coated sites at 0.05 mA cm^{-2} and 1.6 mA cm^{-2} . (d) Optical images of the LLZO pellet surface on the uncoated and aLLZO-coated side recorded at the beginning of the plating-stripping process and after reaching a current density of 1.6 mA cm^{-2} . Magnified image shows a Li filament short-circuiting the Li contacts in the uncoated side of the pellet.

During the plating-stripping process, the surface of the pellet was monitored with an optical microscope in order to observe the nucleation and growth of Li filaments in the bulk ceramic electrolyte. As seen in the voltage plot, high overpotentials are present in both the uncoated and aLLZO-coated test areas, which can be attributed to the geometry of the in-plane measurement and likely poor contact of the evaporated Li due to the lack of externally applied pressure. In the voltage profile of the uncoated pellet, one can observe a continuous spiky behavior, even at the lowest current density, which seems to be related to microshorts

forming across the Li contacts. This phenomenon can be explained by the high polarization leading to a massive injection of electrons through the grain boundaries that promotes the nucleation of Li metal in the interior of the ceramic electrolyte. The spiky behavior of the uncoated site repeats itself with increasing current densities and eventually leads to irreversible shunting of the test device at a current density of 1.6 mA cm^{-2} . In contrast, in the aLLZO-coated side the voltage profile remains stable throughout the plating-stripping process. At high current densities and despite the enormous overpotential, the aLLZO-coated site maintains a stable polarization. The growth of Li filaments and shunting can also be observed in the in-operando optical microscope images recorded during the cycling process (Figure 4.d). In the initial state the space between the Li metal contacts on both the coated and uncoated sides is free of any inhomogeneity. After reaching the plating-stripping current of 1.6 mA cm^{-2} , the uncoated side shows a large Li dendrite connecting both contacts as well as some branches of metallic Li that have grown around the edge of the contacts. Conversely, the aLLZO coated site remains free of Li metal filaments. This experiment demonstrates that the aLLZO coating can prevent the nucleation of Li metal inside the ceramic LLZO and hinder the growth of Li metal dendrites that lead to short-circuiting of the cell.

2.5 Ultrathin solid electrolyte for microbatteries

The aLLZO films here investigated can also be utilized as ultrathin electrolyte for thin-film solid-state batteries. Microbatteries have been investigated since the early 90s and have been developed into a commercial product for powering low-power devices such as IoT sensors, wearables, etc.³⁰ These devices consist of thin-film electrodes (commonly LiCoO_2 as cathode and Li metal as anode) and generally employ lithium phosphorus oxynitride (LiPON) films in the range of microns as solid-state electrolyte.

We fabricated a thin-film battery employing sputtered thin-film LiCoO_2 (LCO) as cathode material and evaporated Li metal as anode. A 70 nm thin aLLZO film was employed as solid electrolyte between the cathode and anode films. To prevent oxidative degradation of

the electrolyte in contact with the LCO (see cyclovoltammetry measurement in Figure S6), a 10 nm LiNbO_3 coating was applied by sputtering to the cathode film prior to the aLLZO deposition. Figure 6.a shows a cross-section SEM image of the microbattery, in which the ultrathin aLLZO electrolyte is shown to conformably cover the LCO cathode film and separate it from the Li metal anode. Note that the poor microstructure of the Li metal is due to the damage produced by the Ga-ion focused ion beam (FIB) employed to prepare the cross section.³¹

Figure 6.b shows the voltage curves of the microbattery upon charge-discharge at current densities ranging from $22 \mu\text{A cm}^{-2}$ (1C) to $220 \mu\text{A cm}^{-2}$ (10C). The voltage profiles show the characteristic plateau at 3.9 V vs Li/Li^+ characteristic of the cathode material employed, indicating unhindered lithium intercalation/deintercalation in and out of the cathode. At lower C rates, overpotentials are moderate (about 50 mV) and as expected, they increase with increasing C rate. The relation between the discharge capacity and the C rate is presented in Figure 6.c. At 1C, the microbattery shows a discharge capacity of $55 \mu\text{A h cm}^{-2} \mu\text{m}^{-1}$, which is equivalent to about 110 mA h g^{-1} assuming an ideal density of the cathode film. At 10C, the microbattery shows a capacity of $39 \mu\text{A h cm}^{-2} \mu\text{m}^{-1}$, a 70% of the capacity at 1C.

To demonstrate the robustness of the ultrathin aLLZO electrolyte, the thin-film battery was cycled with a current density of 0.2 mA cm^{-2} (10C) for 500 cycles, as shown in Figure 6.c. After 500 cycles (about 100 hours operation), the capacity degrades to about 60% of the initial capacity while retaining a stable Coulombic efficiency of about 97.6%. The capacity fading is likely due to interfacial degradation of the electrolyte on the cathode side, but the cell does not show any signs of short circuiting, evidencing high resistance of the aLLZO electrolyte to lithium dendrite formation despite its ultrathin thickness. The high-potential and long-term operation of a microbattery with such an ultrathin sputtered electrolyte is unprecedented and can only be compared to the 90 nm-thick LiPON electrolyte films prepared by atomic layer deposition (ALD) in the work of Pearse et al.³²

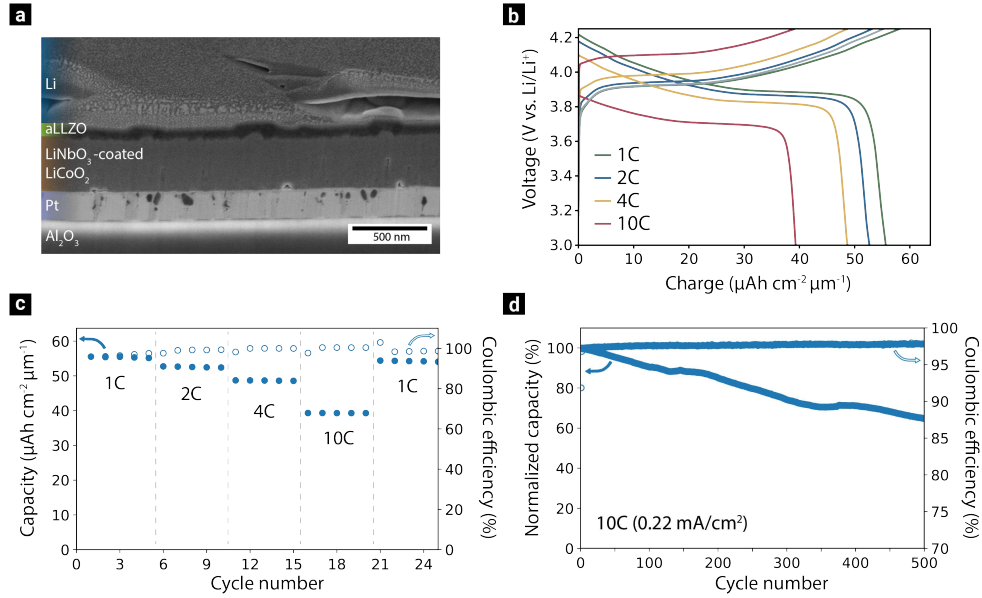


Figure 6: Thin-film solid-state battery with an ultrathin aLLZO electrolyte. (a) Cross-section SEM image of the battery stack. (b) Charge-discharge curves at different C rates (1C = 22 $\mu\text{A cm}^{-2}$). (c) Discharge capacity and Coulombic efficiency of the battery at different C rates. (d) Long-term cycling of the battery over 500 cycles at 10C (0.2 mA cm^{-2})

3 Conclusions

We demonstrate that the amorphous phase of garnet LLZO can act as an ultrathin (< 100 nm) solid electrolyte for solid-state microbatteries as well as a coating for preventing lithium dendrite growth in bulk ceramic electrolytes. The fabrication process presented in this work allows to increase the lithiation of the films and to enhance their ionic conductivity to values approaching $10^{-7} \text{ S cm}^{-1}$. The amorphous nature of the sputtered films results in a grain-boundary-free ultrathin electrolyte that can withstand high current densities without short-circuiting due to lithium filament penetration. Moreover, the low electronic conductivity of $10^{-14} \text{ S cm}^{-1}$ blocks injection of electrons, preventing the nucleation of Li metal inside a coated bulk ceramic electrolyte. We believe that amorphous Li-La-Zr-O coatings can have a significant impact in the development of better solid-state batteries with ceramic electrolytes and lithium metal as anode, allowing higher fast-discharge currents and increasing their lifetime. Future work should focus in implementing and testing this coating material

in bulk solid-state batteries.

Acknowledgement

This work was supported by the Swiss National Science Foundation (grant number 200021_172764), the joint Empa-Fraunhofer ISC project "IE4B" under the ICON funding line, the Strategic Focus Area (SFA) Advanced Manufacturing of the ETH Domain (project "X-Ray Diagnostics"), and the Empa internal project "SUISSE-battery". The TOF-SIMS measurements have been performed in the frame of Swiss Commission for Technology and Innovation (CTI) project (grant number 25592.1PFNM-NM).

Supporting Information Available

Sample preparation and characterization methodology, secondary electron image of FIB-TOF-SIMS crater, 3D reconstructions of sample chemical structure, ToF-SIMS depth profile, electric modulus of the EIS measurements, current transient measurements, extracted charge and ion densities, Arrhenius plots of ionic and electronic conductivities, cyclic voltammetry measurement of a Li/aLLZO/Pt half-cell, area specific resistance during plating-stripping of a symmetric Li/aLLZO/Li cell.

References

- (1) Janek, J.; Zeier, W. G. A Solid Future for Battery Development. *Nat. Energy* **2016**, *1*, 16141.
- (2) Albertus, P.; Babinec, S.; Litzelman, S.; Newman, A. Status and Challenges in Enabling the Lithium Metal Electrode for High-Energy and Low-Cost Rechargeable Batteries. *Nat. Energy* **2018**, *3*, 16.

- (3) Samson, A. J.; Hofstetter, K.; Bag, S.; Thangadurai, V. A Bird's-Eye View of Li-Stuffed Garnet-Type $\text{Li}_7\text{La}_3\text{Zr}_2\text{O}_{12}$ Ceramic Electrolytes for Advanced All-Solid-State Li Batteries. *Energy Environ. Sci.* **2019**, *12*, 2957–2975.
- (4) Wang, C.; Fu, K.; Kammampata, S. P.; McOwen, D. W.; Samson, A. J.; Zhang, L.; Hitz, G. T.; Nolan, A. M.; Wachsman, E. D.; Mo, Y.; Thangadurai, V.; Hu, L. Garnet-Type Solid-State Electrolytes: Materials, Interfaces, and Batteries. *Chem. Rev.* **2020**, *120*, 4257–4300.
- (5) Krauskopf, T.; Richter, F. H.; Zeier, W. G.; Janek, J. Physicochemical Concepts of the Lithium Metal Anode in Solid-State Batteries. *Chem. Rev.* **2020**, *120*, 14463–14477.
- (6) Huang, W. L.; Zhao, N.; Bi, Z. J.; Shi, C.; Guo, X. X.; Fan, L. Z.; Nan, C. W. Can We Find Solution to Eliminate Li Penetration through Solid Garnet Electrolytes? *Materials Today Nano* **2020**, *10*, 100075.
- (7) Hatzell, K. B.; Chen, X. C.; Cobb, C. L.; Dasgupta, N. P.; Dixit, M. B.; Marbella, L. E.; McDowell, M. T.; Mukherjee, P. P.; Verma, A.; Viswanathan, V.; Westover, A. S.; Zeier, W. G. Challenges in Lithium Metal Anodes for Solid-State Batteries. *ACS Energy Lett.* **2020**, *5*, 922–934.
- (8) Han, F.; Westover, A. S.; Yue, J.; Fan, X.; Wang, F.; Chi, M.; Leonard, D. N.; Dudney, N. J.; Wang, H.; Wang, C. High Electronic Conductivity as the Origin of Lithium Dendrite Formation within Solid Electrolytes. *Nat. Energy* **2019**, *4*, 187–196.
- (9) Song, Y.; Yang, L.; Tao, L.; Zhao, Q.; Wang, Z.; Cui, Y.; Liu, H.; Lin, Y.; Pan, F. Probing into the Origin of an Electronic Conductivity Surge in a Garnet Solid-State Electrolyte. *J. Mater. Chem. A* **2019**, *7*, 22898–22902.
- (10) Liu, H.; Cheng, X.-B.; Huang, J.-Q.; Yuan, H.; Lu, Y.; Yan, C.; Zhu, G.-L.; Xu, R.; Zhao, C.-Z.; Hou, L.-P.; He, C.; Kaskel, S.; Zhang, Q. Controlling Dendrite Growth in Solid-State Electrolytes. *ACS Energy Lett.* **2020**, *5*, 833–843.

- (11) Kim, J.-S.; Kim, H.; Badding, M.; Song, Z.; Kim, K.; Kim, Y.; Yun, D.-J.; Lee, D.; Chang, J.; Kim, S.; Im, D.; Park, S.; Kim, S. H.; Heo, S. Origin of Intergranular Li Metal Propagation in Garnet-Based Solid Electrolyte by Direct Electronic Structure Analysis and Performance Improvement by Bandgap Engineering. *J. Mater. Chem. A* **2020**, *8*, 16892–16901.
- (12) Kalita, D.; Lee, S.; Lee, K.; Ko, D.; Yoon, Y. Ionic Conductivity Properties of Amorphous Li–La–Zr–O Solid Electrolyte for Thin Film Batteries. *Solid State Ion.* **2012**, *229*, 14–19.
- (13) Garbayo, I.; Struzik, M.; Bowman, W. J.; Pfenninger, R.; Stilp, E.; Rupp, J. L. M. Glass-Type Polyamorphism in Li-Garnet Thin Film Solid State Battery Conductors. *Adv. Energy Mater.* **2018**, 1702265.
- (14) Westover, A. S.; Dudney, N. J.; Sacci, R. L.; Kalnaus, S. Deposition and Confinement of Li Metal along an Artificial Lipon–Lipon Interface. *ACS Energy Lett.* **2019**, *4*, 651–655.
- (15) Deng, T.; Ji, X.; Zhao, Y.; Cao, L.; Li, S.; Hwang, S.; Luo, C.; Wang, P.; Jia, H.; Fan, X.; Lu, X.; Su, D.; Sun, X.; Wang, C.; Zhang, J.-G. Tuning the Anode–Electrolyte Interface Chemistry for Garnet-Based Solid-State Li Metal Batteries. *Adv. Mater.* **2020**, *32*, 2000030.
- (16) Sastre, J.; Lin, T.-Y.; Filippin, A. N.; Priebe, A.; Avancini, E.; Michler, J.; Tiwari, A. N.; Romanyuk, Y. E.; Buecheler, S. Aluminum-Assisted Densification of Cosputtered Lithium Garnet Electrolyte Films for Solid-State Batteries. *ACS Appl. Energy Mater.* **2019**, *2*, 8511–8524.
- (17) Sastre, J.; Priebe, A.; Döbeli, M.; Michler, J.; Tiwari, A. N.; Romanyuk, Y. E. Lithium Garnet $\text{Li}_7\text{La}_3\text{Zr}_2\text{O}_{12}$ Electrolyte for All-Solid-State Batteries: Closing the Gap between Bulk and Thin Film Li-Ion Conductivities. *Adv. Mater. Interfaces* **2020**, 2000425.

- (18) Priebe, A.; Utke, I.; Pethö, L.; Michler, J. Application of a Gas-Injection System during the FIB-TOF-SIMS Analysis—Influence of Water Vapor and Fluorine Gas on Secondary Ion Signals and Sputtering Rates. *Anal. Chem.* **2019**, *91*, 11712–11722.
- (19) Wagner, R.; Redhammer, G. J.; Rettenwander, D.; Senyshyn, A.; Schmidt, W.; Wilkening, M.; Amthauer, G. Crystal Structure of Garnet-Related Li-Ion Conductor $\text{Li}_{7-3x}\text{Ga}_x\text{La}_3\text{Zr}_2\text{O}_{12}$: Fast Li-Ion Conduction Caused by a Different Cubic Modification? *Chem. Mater.* **2016**, *28*, 1861–1871.
- (20) Gittleson, F. S.; Yao, K. P. C.; Kwabi, D. G.; Sayed, S. Y.; Ryu, W.-H.; Shao-Horn, Y.; Taylor, A. D. Raman Spectroscopy in Lithium-Oxygen Battery Systems. *ChemElectroChem* **2015**, *2*, 1446–1457.
- (21) Kanade, K. G.; Baeg, J. O.; Apte, S. K.; Prakash, T. L.; Kale, B. B. Synthesis and Characterization of Nanocrystallined Zirconia by Hydrothermal Method. *Materials Research Bulletin* **2008**, *43*, 723–729.
- (22) Xu, Z.; Zhao, Q.; Sun, Y.; Ren, B.; You, L.; Wang, S.; Ding, F. Synthesis of Hollow $\text{La}_2\text{O}_3:\text{Yb}^{3+}/\text{Er}^{3+}/\text{Tm}^{3+}$ Microspheres with Tunable up-Conversion Luminescence Properties. *RSC Adv.* **2013**, *3*, 8407–8416.
- (23) Tian, J.; Peng, H.; Xu, X.; Liu, W.; Ma, Y.; Wang, X.; Yang, X. High Surface Area $\text{La}_2\text{Sn}_2\text{O}_7$ Pyrochlore as a Novel, Active and Stable Support for Pd for CO Oxidation. *Catal. Sci. Technol.* **2015**, *5*, 2270–2281.
- (24) Wijaya, O.; Hartmann, P.; Younesi, R.; Markovits, I. I. E.; Rinaldi, A.; Janek, J.; Yazami, R. A Gamma Fluorinated Ether as an Additive for Enhanced Oxygen Activity in Li–O₂ Batteries. *J. Mater. Chem. A* **2015**, *3*, 19061–19067.
- (25) Ren, Y.; Chen, K.; Chen, R.; Liu, T.; Zhang, Y.; Nan, C.-W. Oxide Electrolytes for Lithium Batteries. *J. Am. Ceram. Soc.* **2015**, *98*, 3603–3623.

- (26) Bredar, A. R. C.; Chown, A. L.; Burton, A. R.; Farnum, B. H. Electrochemical Impedance Spectroscopy of Metal Oxide Electrodes for Energy Applications. *ACS Appl. Energy Mater.* **2020**, *3*, 66–98.
- (27) Famprakis, T.; Canepa, P.; Dawson, J. A.; Islam, M. S.; Masquelier, C. Fundamentals of Inorganic Solid-State Electrolytes for Batteries. *Nat. Mater.* **2019**, *18*, 1278–1291.
- (28) Grady, Z. A.; Wilkinson, C. J.; Randall, C. A.; Mauro, J. C. Emerging Role of Non-Crystalline Electrolytes in Solid-State Battery Research. *Front. Energy Res.* **2020**, *8*, 218.
- (29) Kazyak, E.; Garcia-Mendez, R.; LePage, W. S.; Sharafi, A.; Davis, A. L.; Sanchez, A. J.; Chen, K.-H.; Haslam, C.; Sakamoto, J.; Dasgupta, N. P. Li Penetration in Ceramic Solid Electrolytes: Operando Microscopy Analysis of Morphology, Propagation, and Reversibility. *Matter* **2020**, *2*, 1025–1048.
- (30) Dudney, N. J. Solid-State Thin-Film Rechargeable Batteries. *Materials Science and Engineering: B* **2005**, *116*, 245–249.
- (31) Lee, J. Z.; Wynn, T. A.; Schroeder, M. A.; Alvarado, J.; Wang, X.; Xu, K.; Meng, Y. S. Cryogenic Focused Ion Beam Characterization of Lithium Metal Anodes. *ACS Energy Lett.* **2019**, *4*, 489–493.
- (32) Pearse, A. J.; Schmitt, T. E.; Fuller, E. J.; El-Gabaly, F.; Lin, C.-F.; Gerasopoulos, K.; Kozen, A. C.; Talin, A. A.; Rubloff, G.; Gregorczyk, K. E. Nanoscale Solid State Batteries Enabled by Thermal Atomic Layer Deposition of a Lithium Polyphosphazene Solid State Electrolyte. *Chem. Mater.* **2017**, *29*, 3740–3753.

Figures

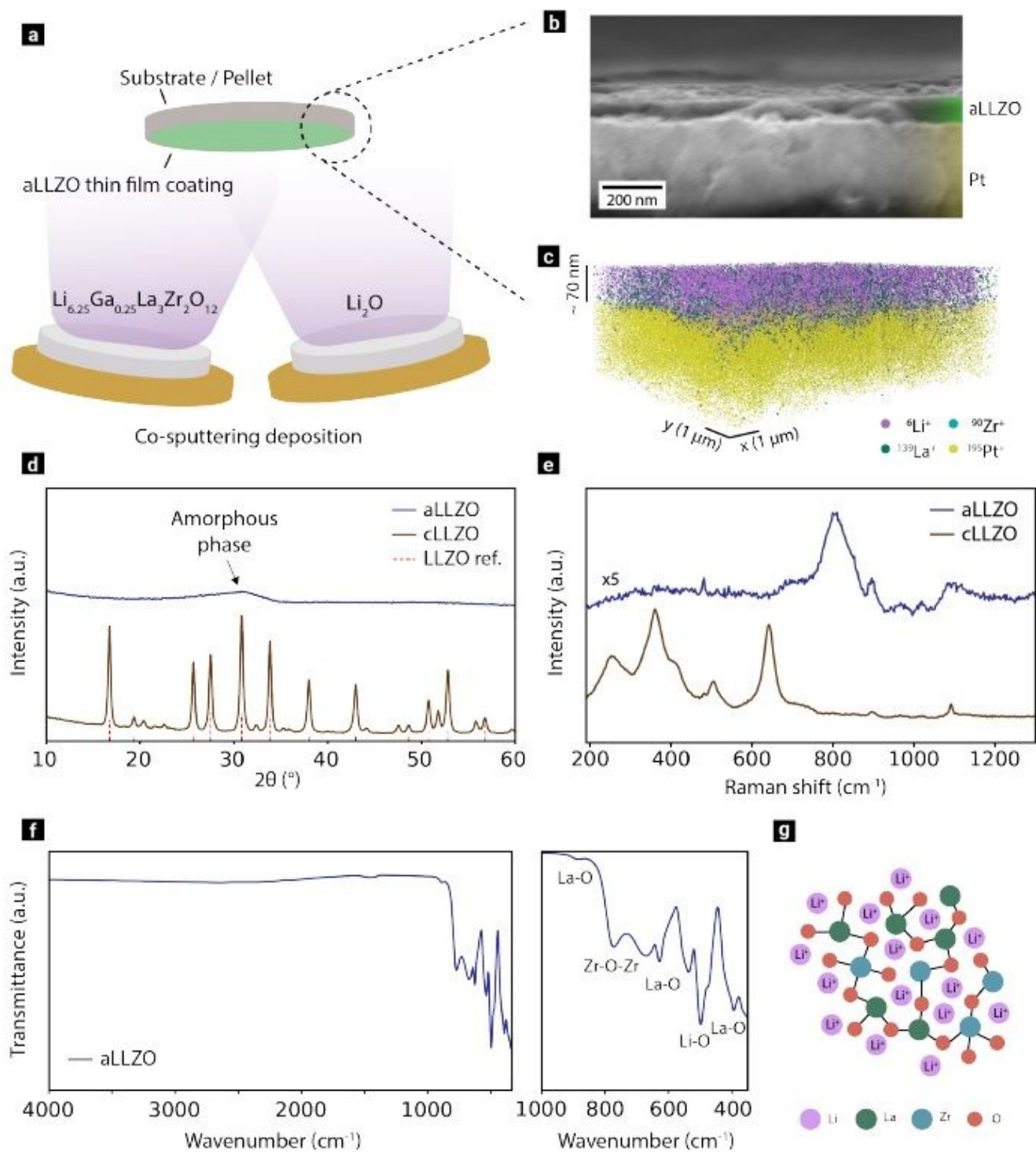


Figure 1

Morphological, phase and chemical characteristics of the amorphous Li-La-Zr-O ultrathin films. (a) Schematic of the co-sputtering deposition process employed to prepare overlithiated amorphous Ga-doped Li-La-Zr-O (aLLZO) coatings. (b) Cross-section SEM image of the aLLZO film on a Pt-coated Si

substrate. (c) Elemental tomogram obtained by GIS-assisted FIB-ToF-SIMS of an aLLZO film deposited on Pt-coated Si. (d) XRD diffractograms of an aLLZO film and a crystallized LLZO (cLLZO) film on single-crystal MgO. A reference pattern for LLZO (ICSD 430603) is included. (e) Raman spectra of the aLLZO and crystallized LLZO films on MgO single crystal substrates. (f) FT-IR transmittance spectrum of the aLLZO film. (g) Representation of the chemical structure of the amorphous Li-La-Zr-O.

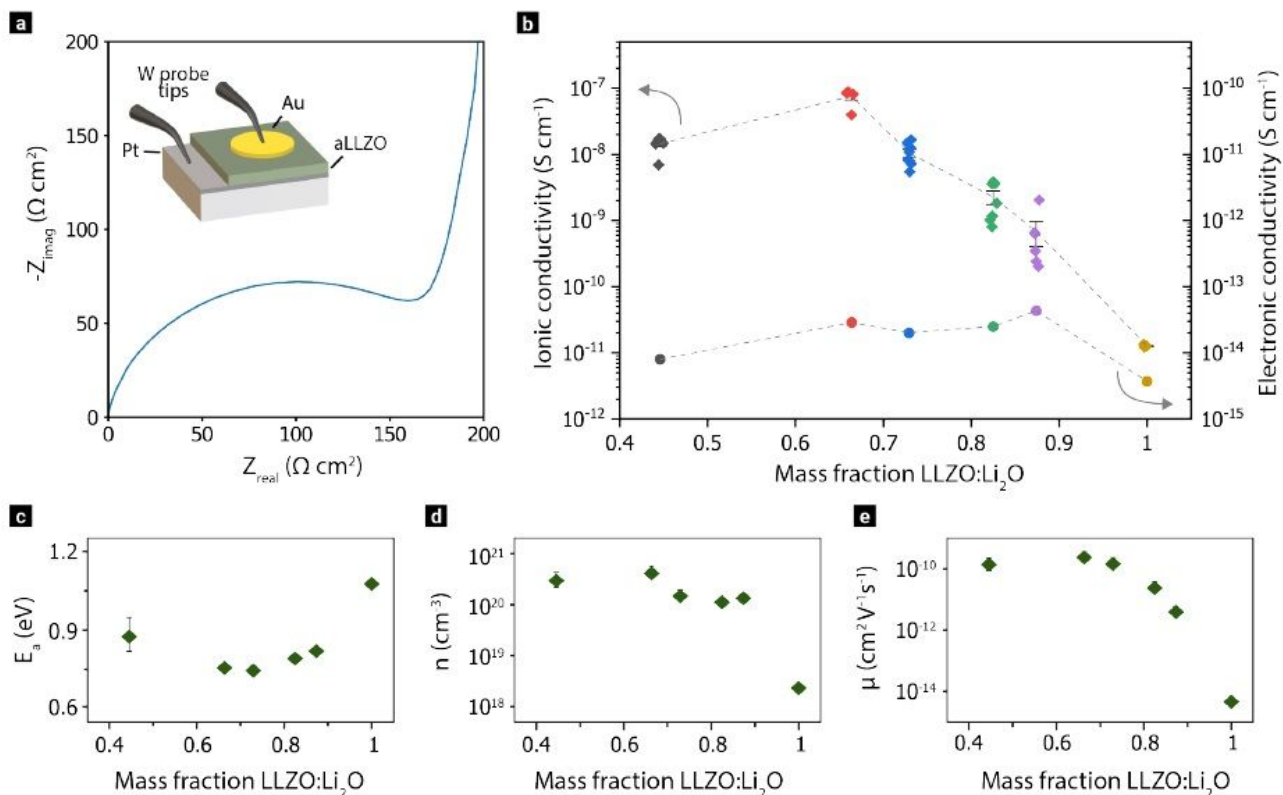


Figure 2

Ionic and electronic transport dynamics of the aLLZO ultrathin films. (a) Nyquist plot of the impedance spectra of an aLLZO film measured with blocking electrodes at room temperature. Inset shows a schematic of the device geometry. (b) Ionic and electronic conductivities of aLLZO films prepared with different mass fractions of LLZO and Li_2O . (c) Activation energy of the ionic conductivity, (d) mobile Li^+ concentration and (e) Li^+ mobility of aLLZO films with different amounts of Li_2O based on the mean of three measurements each.

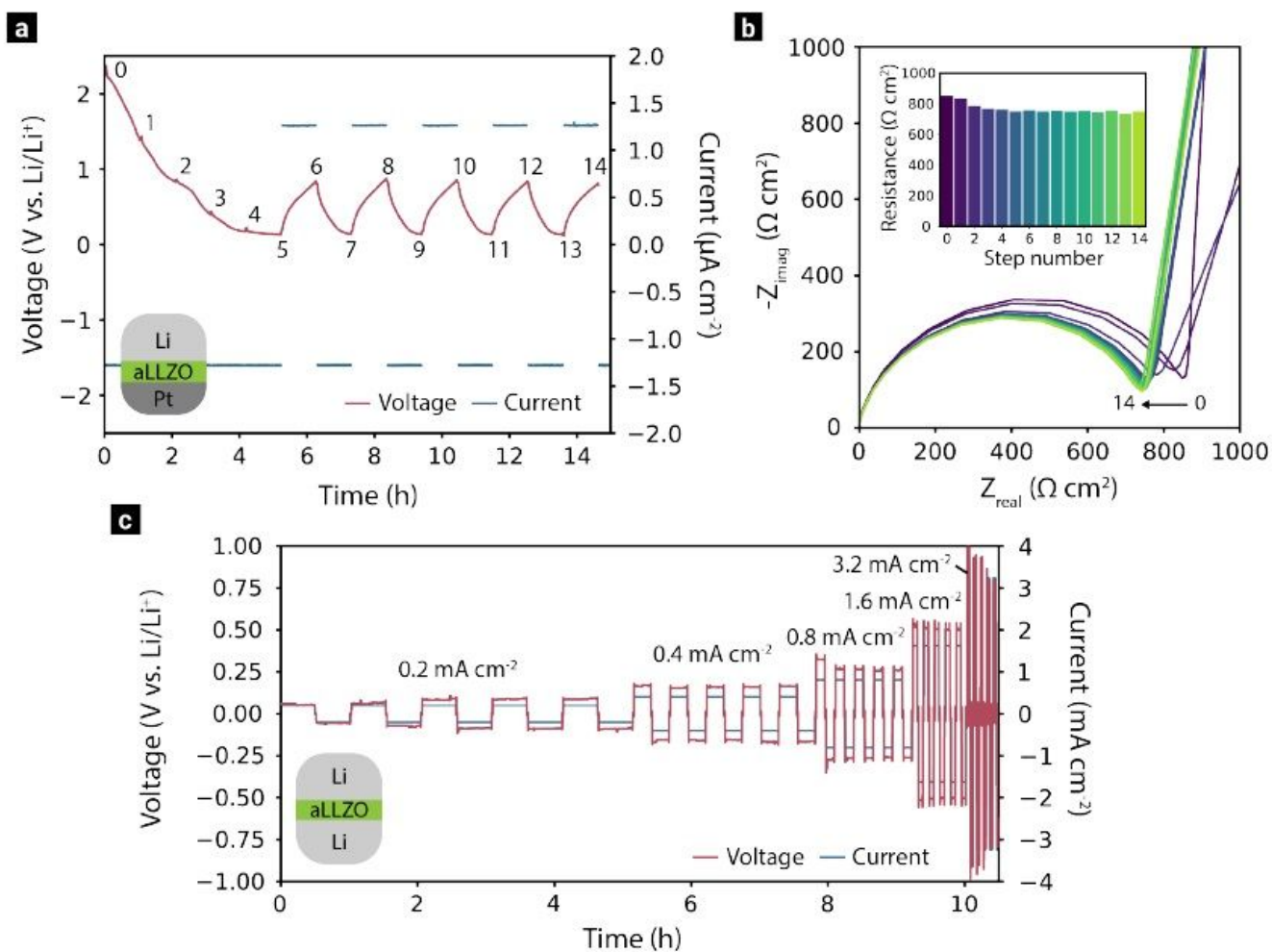


Figure 3

Li stability and short circuit resistance of the aLLZO films. (a) Galvanostatic response of an aLLZO electrolyte film upon electrochemical transport of Li^+ from a Li counter electrode to a Pt working electrode and reversely. Numbers along the plot line indicate the points at which impedance spectroscopy measurements were carried out. (b) Nyquist plot of the impedance response of the aLLZO film in contact with Li metal after multiple steps of plating and stripping. Inset shows the evolution of the electrolyte resistance extracted from the impedance spectra. (c) Galvanostatic response of an aLLZO electrolyte film in a symmetric Li/Li cell configuration. Forward and reverse current densities ranging from 0:2 mA cm^{-2} up to 3:2 mA cm^{-2} were applied in steps of 0:1 mAh cm^{-2} .

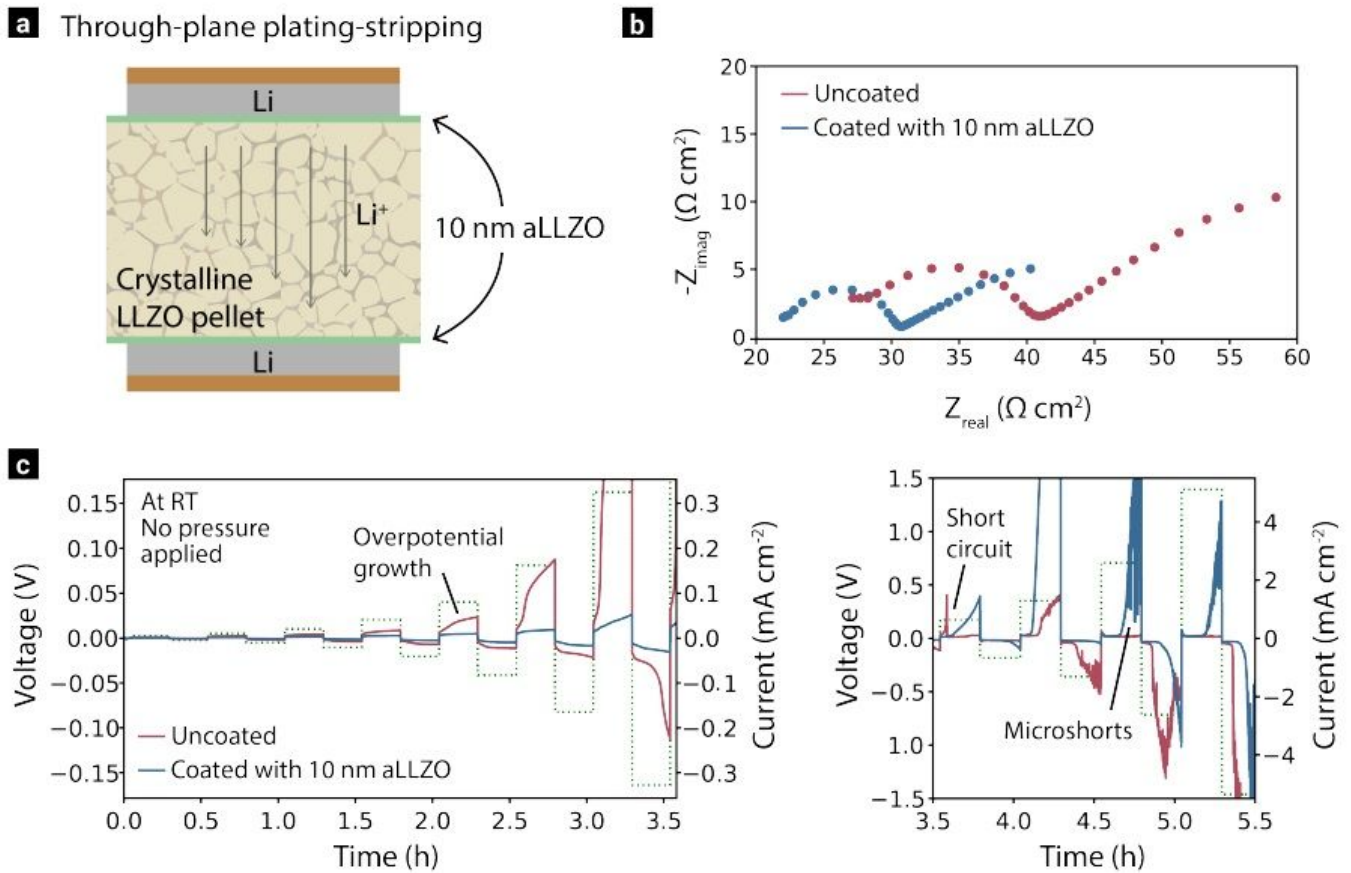


Figure 4

Ultrathin aLLZO coating inhibits the growth of Li dendrites in bulk crystalline LLZO electrolyte. (a) Schematic of the through-plane Li/aLLZO/LLZO/aLLZO/Li configuration employed to determine the critical current density. (b) Nyquist plot of the impedance response of the uncoated and aLLZO-coated LLZO pellets. (c) Applied current density (dashed line) and voltage response (solid lines) during symmetric galvanostatic cycling of the uncoated and aLLZO-coated LLZO pellets at RT without external pressure applied. Forward and reverse current densities ranging from $5 \mu\text{Acm}^{-2}$ up to $5:1 \text{ mAcm}^{-2}$ were applied in steps of 30 min.

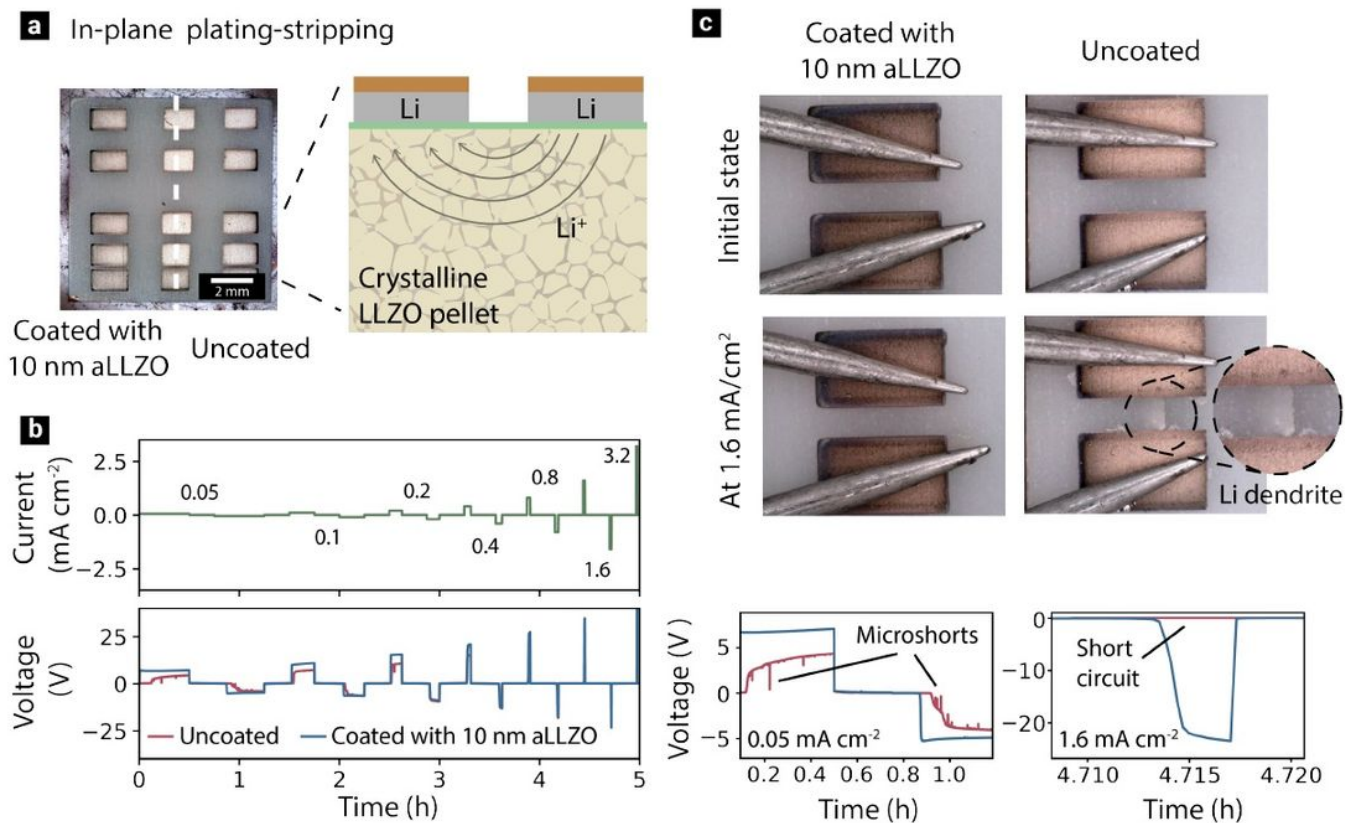


Figure 5

Visualizing dendrite growth in bulk crystalline LLZO electrolyte. (a) Optical picture and schematic of the in-plane geometry employed to visualize the formation of dendrites upon Li plating-stripping. Half of a 10 x10 mm LLZO pellet was coated with 10 nm aLLZO and Li metal contacts with Cu as current collector were deposited on both sides of the pellet. (b) Nyquist plot of the impedance response between two of contacts spaced 0.5 mm on the aLLZO-coated side. (c) Current and voltage response during symmetric galvanostatic cycling between two Li metal contacts. Forward and reverse current densities ranging from 0:05 mA cm^{-2} up to 3:2 mA cm^{-2} were applied in steps of 25 $\mu\text{Ah cm}^{-2}$. Subplots show a zoom-in of the polarization in the uncoated and coated sites at 0:05 mA cm^{-2} and 1:6 mA cm^{-2} . (d) Optical images of the LLZO pellet surface on the uncoated and aLLZO coated side recorded at the beginning of the plating-stripping process and after reaching a current density of 1:6 mA cm^{-2} . Magnified image shows a Li filament short-circuiting the Li contacts in the uncoated side of the pellet.

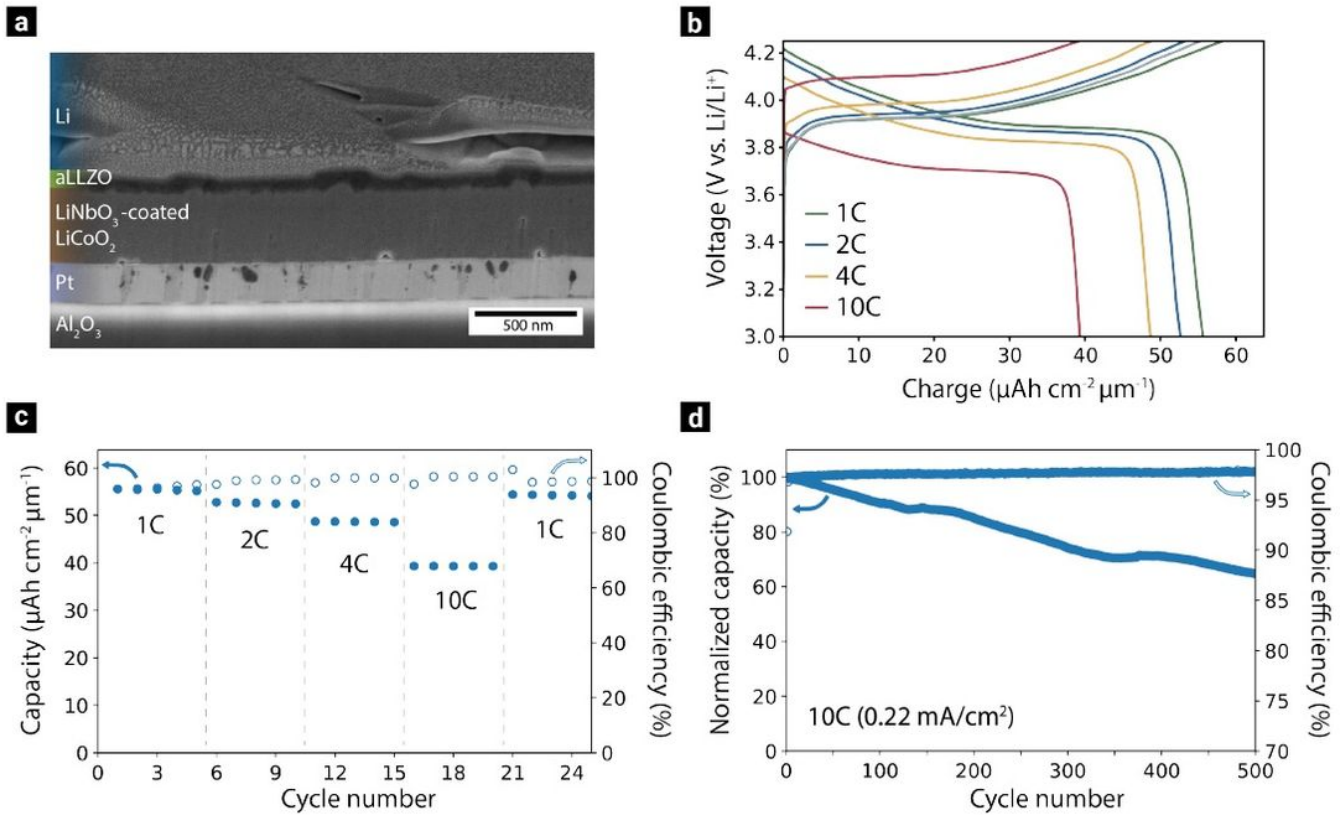


Figure 6

Thin-film solid-state battery with an ultrathin aLLZO electrolyte. (a) Cross-section SEM image of the battery stack. (b) Charge-discharge curves at different C rates (1C = 22 μAcm^{-2}). (c) Discharge capacity and Coulombic efficiency of the battery at different C rates. (d) Long-term cycling of the battery over 500 cycles at 10C (0.22 mAcm^{-2})

Supplementary Files

This is a list of supplementary files associated with this preprint. Click to download.

- [supplementaryinformationaLLZO.pdf](#)